Application of ultrasound techniques to liquid-liquid dispersed flows

Fria Hossein [a], Paula S.C. Farias [b], Xueyu Qi [a], Panagiota Angeli [a,*]

[a] *ThAMeS Mutiphase, Department of Chemical Engineering, University College London, Torrington Place, London WC1E 7JE, UK*
[b] *Department of Mechanical Engineering, PUC-Rio, Rio de Janeiro, Brazil*

ARTICLE INFO

ABSTRACT

This paper delineates the development and application of non-intrusive diagnostic ultrasound (US) techniques for the measurement of the drop size distribution (DSD) and the drop volume fraction in dispersed liquid-liquid flows. The techniques used here are based on the measurement of the speed and the attenuation coefficient of the propagated ultrasound wave. To validate the results of the ultrasound measurements, a planar laser induced fluorescence (PLIF) technique was used to image the dispersed phase at the same time and location as the ultrasound transducers. For the tests, a silicon oil and a glycerol/water mixture, with the same refractive index as the oil, were used. The experiments were carried out in a stirred vessel with the impeller placed either just below the oil/aqueous mixture interface or at 25 mm below the interface and rotated at speeds of 300–400 rpm. The dispersed oil volume fractions measured by both the US and PLIF techniques were in excellent agreement and varied between 0.53% to 4.2%. Good agreement between the two techniques was also found for the drop size distributions. For the conditions investigated, the drop size ranged from 0.25 mm to 2 mm. The results indicated that the developed ultrasound technique is a powerful tool for characterising dispersed phases in liquid-liquid flows.

1. Introduction

Dispersions of two immiscible liquids have very wide applications in many industrial sectors including manufacturing and energy and in everyday products such as food, cosmetics, chemicals, and pharmaceuticals (Martínez et al., 2021). In such processes, the distributions of the droplet sizes and of the volume fraction are key parameters that affect mixing, mass and heat transfer (Russell et al., 2019). An inadequate understanding of the dynamics of dispersed flows can lead to overdesign of equipment and have profound effects on the quality of the final products (Simmons and Hanratty, 2001). Measurements of droplet size distribution and drop volume fraction further contribute to the understanding of the droplet coalescence and breakup phenomena in dispersions and to the development of predictive models (Bowler et al., 2020; Liu et al., 2016; Rodriguez et al., 2019). Rave et al. (2022) investigated liquid-liquid mixtures in a baffled stirred vessel and measured the drop size distributions by using an intrusive shadowgraphic probe. Castellano et al. (2019) developed a model for drop breakage and coalescence kernels valid for the entire spectrum of turbulence and validated against experimental data.

The current techniques available to study liquid-liquid dispersed flows rely on sensors that are based on conductivity or capacitance (Bowler et al., 2020) of the phases, on optical properties (Prakash et al., 2019), or on local heat transfer such as the hot film anemometer (Tas-Koehler et al., 2022). Many of these sensors are intrusive and can disturb the flow field, thus affecting the accuracy of the measurements (Yelpale et al., 2021). Moreover, spatial resolution and the calibration procedure are common drawbacks in the application of electrical sensors (Wallace et al., 2012). Examples of tomographic techniques applied to liquid-liquid systems include electrical capacitance tomography- ECT (Wu et al., 2018), and electromagnetic tomography - EMT (Vauhkonen et al., 2019), which measures the mean flow velocity. These techniques have a good accuracy but reduced spatial resolution and complex data processing methodologies (Bieberle et al., 2013; Wang et al., 2011).

Quantitative measurement of liquid dispersions based on imaging have followed the evolution of digital cameras, image processing capacity, high energy and frequency lasers (Angeli et al., 2019). Examples of optical techniques include high speed imaging and laser based approaches (Charogiannis and Markides, 2014) such as Planar Laser Induced Fluorescence – PLIF (Farias et al., 2012; Rodríguez and Shedd, 2004) Laser Doppler Velocimetry - LDV (Bouillard et al., 2001), and Particle Image Velocimetry – PIV (Ayala et al., 2022). These techniques can only be applied when the test section is transparent, while light

* Corresponding author.
E-mail address: p.angeli@ucl.ac.uk (P. Angeli).

Nomenclature		K	Complex wave number in dispersed phase
		K_w	Complex wave number in continuous phase
C	Ultrasound speed	φ	Droplet volume fraction
C_s	Ultrasound speed in dispersion	A_n	Scattering coefficient
C_{gw}	Ultrasound speed in water/glycerol	A	Extinction coefficient
f	Wave frequency	F	Discrete frequency distribution
α_s	Attenuation coefficient in dispersed phase	γ	Lagrange multiplier
α_w	Attenuation coefficient in continuous phase	H	Smoothing matrix
A_o	Signal amplitude in dispersion	r	Drop radius
A_1	Signal amplitude in continuous phase	ρ_o	Density of dispersed phase (silicone oil)
ω	Angular frequency	ρ_{gw}	Density of continuous phase
i	Imaginary unit	D	Inner diameter of stirred vessel

scattering at interfaces limits the dispersed phase volume fractions that can be studied. To increase the volume fractions, liquids with matching refractive index should be used, which however, limit the range of liquids that can be studied (Vauhkonen et al., 2019). Often, seeding of the phases with tracer particles to obtain velocity fields, or use of fluorescent dyes to better discriminate the phases are used (Charogiannis et al., 2019). Techniques based on radiation such as magnetic resonance imaging (MRI), and gamma ray or X-ray attenuation are relying on the density differences of the materials; for liquid-liquid flows where the density differences between the two phases are small, their application is limited (Iannello et al., 2020).

In the presence of these limitations, ultrasound techniques have emerged as powerful alternatives for dispersed flow measurements, providing fast, low-cost measurements that do not involve ionizing radiation, and can be applied to non-transparent fluids and test sections. The propagation of ultrasound waves through a liquid containing multiple microbubbles was studied by Kikuchi et al. (2022). They introduced an extension of acoustic theory for single encapsulated bubble to multiple bubbles and studied the effect of encapsulated bubbles and shell compressibility on the ultrasound wave propagation. In previous studies, the ultrasound Doppler Effect has been applied to dispersed flows for velocity measurements (Dong et al., 2015; Murakawa et al., 2020). Ultrasound techniques have been applied to ionic liquids (KCL, NACL, NAOH, MGCL2) to analyse atomic masses, to colloidal suspensions to measure the physiochemical properties of nanoparticles, including charge density and concentration (Hossein, 2019; Hossein and Wang, 2020). We recently demonstrated their applicability to dense particle suspensions, in fluidized bed systems (Hossein et al., 2022). The ultrasound wave propagation speed and attenuation depend on the properties of both continuous and dispersed phases such as: density, compressibility, and temperature. The technique was used to obtain concentration (by measuring the sound speed or attenuation), and size distributions (by measuring the attenuation) of the dispersed phase in multiphase flows. From the frequency shift of the emitted ultrasound wave through the particle suspension, the velocity profiles of the particles were also calculated (Hossein et al., 2022). Some of the benefits of ultrasound based techniques are: a) they are based on fundamental theory and calibration is not required, when the physical constants of the phases are known; b) they can characterise more than one phases simultaneously; c) they can be used with highly concentrated dispersions and with opaque systems; d) the impact of dispersed phase shape can be reduced by selecting the right frequencies (Povey, 2013).

The signal post processing of the ultrasound-based techniques can be complex, particularly when the sound wave travels through multiple interfaces in multiphase mixtures. Sound wave properties are dependent on temperature and humidity, which can make the development of the techniques challenging in systems where temperature or humidity are not under control. Furthermore, ultrasound techniques have relatively low spatial resolution. One way to improve resolution is to increase the ultrasound frequency; this, however, results in decreasing wave

penetration depth in the flow (Hossein et al., 2021). Despite these drawbacks, ultrasound techniques can offer fast characterisation of multiple flow features, particularly suitable for online measurements and process control.

In this work we developed and applied ultrasound techniques and postprocessing methodologies to characterise drop size distribution (DSD) and drop volume fractions (V_f) in a liquid-liquid dispersion formed in a stirred vessel. The ultrasound methods used here are based on the measurement of the attenuation coefficient at different excitation frequencies, to measure the drop size distribution, and of the ultrasound velocity, to obtain drop volume fractions. For the validation of the ultrasound results, Planar Laser Induced Fluorescence (PLIF) was used to capture time resolved images of the drops at the same time and location as those of the ultrasound transducers. We chose to carry out the studies in a stirred vessel as it allows the simultaneous application of both techniques and the easy variation of operating conditions. In the following sections, the materials used and the experimental setups for both the ultrasound and the PLIF measurements are discussed. Section 3 details the data post-processing for both techniques, and Section 4 provides the results and discussions. In Section 5, the conclusions are summarized.

2. Experimental methodology

2.1. Experimental setup

Dispersions of oil in water were generated in a cylindrical stirred vessel made of acrylic with a diameter of 50 mm, which was enclosed in a squared acrylic box. A schematic diagram of experimental setup with the ultrasound and PLIF is given in Fig. 1a, while the vessel dimensions are detailed in Fig. 1b.

To minimize optical distortions through curved walls, the box was filled with glycerol (refractive index 1.47), which has almost the same refractive index as the acrylic walls (refractive index 1.49). For the experiments, a silicon oil (density 915 kg/m^3 and viscosity 0.0046kg/ms) was selected as the dispersed phase and a 49% w/w mixture of glycerol in distilled water (density 1124 kg/m^3 and viscosity 0.0044 kg/ms) was used as the continuous phase. Both immiscible liquid phases had the same refractive index, equal to 1.39, and their properties are presented in Table 1.

The dispersed phase size distribution in a stirred vessel is related to the properties of the phases and the operating conditions of the mixing system. In the present work, the rotational speed and position of the impeller were varied to obtain a wide range of dispersed phase sizes. Two impeller positions were chosen, named Case 1 and Case 2. In Case 1, the impeller was placed just below the oil/water interface, and in Case 2 the impeller was positioned approximately 25 mm below the oil/water interface. For Case 1 the impeller rotation speed was set at 300 rpm, 350 rpm, and 400 rpm. For Case 2 the impeller rotation speed was set only at 350 rpm and 400 rpm, as with this setup uniform dispersions were not
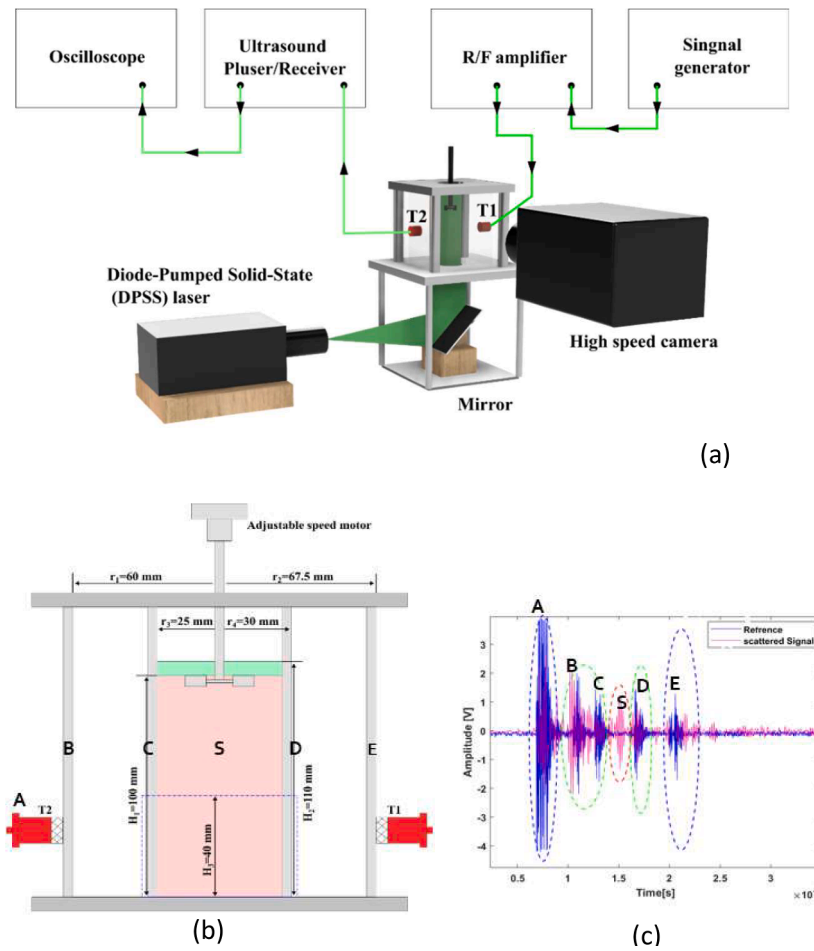
(a)

(b)

(c)

Fig. 1. (a) Experimental setup and ultrasound circuit connections (T1-transmitting transducer, T2-receiving transducer. (b) Schematic diagram of the stirred vessel. (c)Waveform of the ultrasonic spectrum (Reference signal (blue) being the one propagated through continuous phase only and the scattered signal (pink) is the one propagated through the dispersion).

Table 1
The list of physical properties of both continuous and dispersed phases that are used in this work at room temperature.

Physical properties	Silicone oil	Water/Glycerol
Density ($kg/m3$)	913	1124.71
Viscosity (kg/ms)	0.0046	0.0044
Refractive Index (-)	1.39	1.39
Sound Speed (m/s)	1014	1670
Acoustic Impedance MPa	0.93	1.88

achieved at lower rotation speeds. Measurements of the droplet volume fraction and droplet size distribution were conducted with both ultrasound and PLIF techniques, at the same time and axial location, at 40 mm above the bottom of the vessel.

2.2. PLIF set up

We employed the non-intrusive Planar Laser Induced Fluorescence (PLIF) technique to provide time-resolved images to characterise the dispersed oil phase in the stirred vessel and compare against the ultrasound measurements. Since the refractive index between the two phases was matched to reduce optical reflections, the fluorescent dye Rhodamine B was dissolved into the continuous aqueous phase to allow for the optical separation of the two phases (Rodríguez and Shedd, 2004). The fluorescent material was excited by a green light sheet (527 nm wavelength) emitted by a diode-pumped solid-state (DPSS) continuous laser

(see Fig. 1a). A high-pass optical filter with a cut-off wavelength of 560 nm was used in front of the camera lens to block the laser light scattered by the drops and acrylic walls. Hence, the camera only registered the 610 nm light emitted by the fluorescent continuous phase. The longitudinal side view images measuring 1024 $\times$ 1024 pixels with a spatial resolution of 18.3 $pixels/mm$ were captured at an axial position located at 40 mm above the bottom of the vessel using a high-frame-rate digital video camera (Photron) at an acquisition frequency of 250 Hz. Cylindrical (-25 mm) lens and a collimator were used to transform the circular beam into a planar light sheet (1.5 mm thick) and illuminate the longitudinal area of the vessel. The camera equipped with 105 mm Nikkor focal distance lens was mounted orthogonally to the light sheet plane. Due to the camera memory limitation, the acquisition time was limited to 42 s at the maximum resolution of the camera. Measurements of the drop size distribution involved a large number of instantaneous images; thus, in-house routines were developed in MATLAB® to detected automatically the dispersed phase drops using digital image processing.

2.3. Ultrasound set up

A schematic of the equipment used for the ultrasound measurement setup is shown in Fig.1a. Ultrasonic transducers used in these experiments were manufactured by Sonatest (RTD2250 3/4″ in diameter with resonance frequency of 5 MHz). The ultrasound signals were generated via a function generator (33500B, Keysight), while the emitted signals were amplified by 30 dB with an RF amplifier (TS500-C, Accel

Instruments). Signals were sent through the stirred vessel via transducer T_1 and the propagated signals were sensed by transducer T_2, and collected via the ultrasound pulser/receiver. The received signal is attenuated with respect to the transmitted one and for this reason, the signal is amplified up to 65 dB by the ultrasound pulser/receiver. Finally, the digitized signal is captured by an oscilloscope (Keysight-DSOX3014T) and downloaded to a computer for further signal post processing.

Experimentally, we have used two ultrasonic measurement methods; *ultrasound propagation speed*, to calculate the drop volume fraction and *ultrasound attenuation coefficient spectroscopy* to measure the drop size distribution. The ultrasound wave propagation speed depends on the density and compressibility of both the continuous and dispersed phases and the concentration of the dispersed phase in the mixture. This method can therefore be used to measure the concentration of the dispersed phase in two liquid flows. To measure the ultrasound speed in a mixture, a reference signal is required, which is taken when the vessel is filled with the continuous phase (water/glycerol) only. To calculate the ultrasound speed the following equation can be used:

$$C = \frac{D}{t} \tag{1}$$

where, C is the sound speed in the continuous phase, t is the time that the sound wave travels from T1 to T2 (or the arrival time of the propagated sound wave), and D is the vessel diameter, along which the ultrasound wave travels.

As the ultrasound travels through a dispersion, various interactions take place between the waves and the phases, which result in the attenuation of the ultrasound wave and the reduction of its amplitude. These include viscous dissipation (the oscillation of droplets due to the density difference between droplets and continuous phase), absorption, reflection and scattering losses. Scattering is the main cause of attenuation in liquid-liquid dispersions and is caused by the density differences between the droplet and the surrounding liquid. The attenuation coefficient, α, of an ultrasound wave with certain frequency, propagated through a dispersion over the vessel diameter D can be obtained by Eq. (2),

$$\alpha = -\frac{1}{D} \ln\left(\frac{A_o}{A_1}\right) \tag{2}$$

where, A_o is the attenuated signal amplitude and A_1 is the reference signal amplitude.

To analyse the droplet size distribution, a pulsed ultrasound wave at different excitation frequencies of 0.5, 1, 1.5, 2, 2.5, 3, 3.5, 4 *MHz* was generated. A reference amplitude is also required for each frequency, and this was obtained by sending the signal through the continuous phase (water/glycerol) only. An example of the reference signal amplitude spectrum, A_1, at various excitation frequencies is shown in Fig. 2.

3. Data post-processing

3.1. Ultrasound

3.1.1. Ultrasound for droplet volume fraction

Two models have been proposed by (Urick, 1947; Atkinson and Wells, 1977) to obtain the dispersed phase volume fraction from ultrasound speed measurements. Both models assumed that the scattering effect is negligible when the wavelength of the emitted sound wave is much longer than the characteristic size of the dispersed phase. The sound wave was emitted with frequency of 0.5*MHz* so that the droplet sizes were much smaller than the wavelength (3.2 mm). Through this section the silicone oil and water/glycerol solution are represented with the subscripts o and gw, respectively. From the combination of both models (see Appendix I) the following quadratic equation Eq.3 is
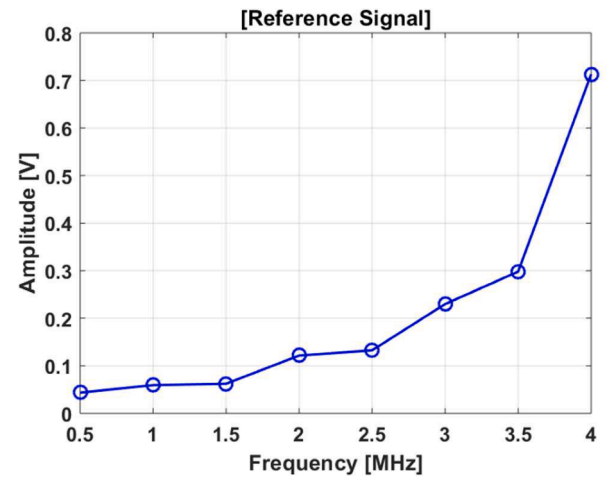

Fig. 2. Amplitude of the reference signal spectrum for various excitation signal frequencies.

developed, which is used to calculate the dispersed phase volume fraction, φ:

$$\varphi = \frac{-B \pm \sqrt{B^2 - 4AD}}{2A} \tag{3}$$

where,

$$A = \left(\left(\frac{C^2}{C_{gw}^2}\right) - \frac{\rho_o}{\rho_{gw}}\left(\frac{C^2}{C_{gw}^2}\right)\right)\left(1 - \frac{\rho_o}{\rho_{gw}}\right)$$

$$B = 2\frac{\rho_o}{\rho_{gw}}\left(\frac{C^2}{C_{gw}^2}\right) - \left(\frac{C^2}{C_o^2}\right) + \left(\frac{\rho_o}{\rho_{gw}}\right)^2\left(\frac{C^2}{C_{gw}^2}\right) + 2\frac{\rho_o}{\rho_{gw}}\left(1 - \left(\frac{C^2}{C_o^2}\right) - \frac{\rho_o}{\rho_{gw}}\right)$$

$$D = \frac{\rho_o}{\rho_{gw}}\left(1 + 2\frac{\rho_o}{\rho_{gw}}\right)\left(1 - \left(\frac{C^2}{C_{gw}^2}\right)\right)$$

where, C is the sound speed in the mixture, C_{gw}, is the sound speed in the continuous phase (water/glycerol), C_o is the sound speed in the dispersed phase (silicone oil), ρ_{gw} is the density of the continuous phase (water/glycerol), and ρ_o is the density of the dispersed phase (silicone oil). Eq. (3) is based on the assumption that if the sound wavelength used here is larger than the drop size then the multiple scattering effect can be neglected (Chaudhuri A et al., 2014). We have previously tested this formula to dispersed systems of solids suspended in liquids at a wide range of volume fractions from 27% to 70%. where we found excellent agreement (see Hossein et al., 2022).

3.1.2. Ultrasound for drop size distribution

The ultrasound attenuation in dispersions depends on the thermophysical properties of the component phases, the drop size, drop volume fraction, and the emission frequency of the ultrasound wave. The thermophysical properties include velocity of the sound wave, as well as density, thermal expansion coefficient, heat capacity, thermal conductivity and viscosity of both phases.

In a dispersion, the main cause of attenuation is scattering and this is related to the size and density of the droplets (McClements, 1996). Also in dispersions, the sound wave is scattered by multiple droplets (multiple scattering). Theoretically, the following equations can be used to calculate multiple scattering. The complex wave number (a complex wave consists of more than one sine waves) in a dispersed phase, K, is given by:

$$K = \frac{\omega}{C_o} + i\alpha_o \tag{4}$$

where, C_o is the sound speed in the dispersed phase, α_o is the attenuation coefficient of the dispersed phase, $\omega = 2\pi f$ is the angular frequency of the emitted wave, and f is the frequency of the emitted wave. In concentrated systems the interaction between droplets becomes significant and the multiple scattering relations should be used (Waterman and Truell, 1961)

$$\left(\frac{K}{K_{gw}}\right)^2 = 1 + \frac{4\pi N f(1)}{K_{gw}^2} + \frac{4\pi^2 N^2}{K_{gw}^4}\left(f(1)^2 - f(2)^2\right) \qquad (5)$$

where, $K_{gw} = \frac{\omega}{C_{gw}} + i\alpha_{gw}$, C_{gw} is the ultrasound speed in the continuous phase (water/glycerol mixture), α_{gw} is the ultrasound attenuation in the continuous phase, φ is the droplet volume fraction, N is the number density of the droplets ($N = \frac{3\varphi}{4\pi r^3}$), r is the droplet radius, while the far field scattering amplitudes $f(1)$, and $f(2)$ are given by:

$$f(1) = \frac{1}{iK_{gw}}\sum_{n=0}^{\infty}(2n+1)A_n \qquad (6)$$

$$f(2) = \frac{1}{iK_{gw}}\sum_{n=0}^{\infty}(-1)^n(2n+1)A_n \qquad (7)$$

where, n is the order of spherical harmonics, and A_n are the scattering coefficients (McClements, 1996); see Appendix II. The overall attenuation coefficient, α, for a dispersion with volume fraction φ, drop radius r_j for $j = 1, 2, \ldots, N$, is given by:

$$\alpha = \frac{3\varphi}{2K_{gw}^2}\sum_{j=1}^{N}\frac{q_j}{r_j^3}\sum_{n=0}^{\infty}(2n+1)Re[A_n] \qquad (8)$$

where q_j is the volume fraction of drops with size in the ranges of $[r_j + r_{j+1}]$. Eq. (8) is the theoretical basis for drop size measurements using ultrasound attenuation coefficient spectra. The attenuation coefficient spectra can be given in a matrix form as:

$$G = MF \qquad (9)$$

where, G, is the attenuation coefficient matrix measured at different excitation frequencies, F is the discrete drop size frequency distribution, M is the scattering coefficient matrix as given by (Jia et al., 2019), and

$$\frac{\alpha}{G} = \underbrace{\frac{3\varphi}{2K_{gw}^2}\sum_{n=0}^{\infty}(2n+1)Re[A_n]}_{M}\underbrace{\sum_{j=1}^{N}\frac{q_j}{r_j^3}}_{F} \qquad (10)$$

where, A_n is the scattering coefficient (McClements, 1996); see Appendix II. The drop size distribution mathematically can be calculated from the inverse of Eq. (9) and is given by:

$$F = M^{-1}G \qquad (11)$$

The solution of Eq. (10) tends to be unstable and ill posed problem. To overcome this, a smooth matrix H and a regularization factor γ are introduced (Su et al., 2008) as follows

$$F = \left(M^T M + \gamma H\right)M^T G \qquad (12)$$

A smooth matrix H is a filter to reduce the noise, while γ is the Lagrange multiplier used to find local minima and maxima values. The solution of F represents the droplet size distribution.

In the matrix notation of Eq.12, γ determines the relative weight given to the smoothing matrix H. The inverse of the scattering coefficient matrix M^{-1} provides an efficient smoothing matrix (Riebel and Löffler, 1989) so that Eq.12 can be presented as $F = (M^T M + \gamma(M^{-1}))M^T G$. The value of γ can be determined by the prescribed error magnitude $\sum E^2 = (MF - G)^T(MF - G)$. The usual procedure for applying this equation is to choose several values for γ in equation $[F = (M^T M + \gamma(M^{-1}))M^T G]$ and then calculate F. The calculated F values are then used in $[\sum E^2 = (MF - G)^T(MF - G)]$ to obtain the $\sum E^2$ values. The value of $\gamma = 0.00312$ which gave the least error $\sum E^2$ was chosen.

The attenuation coefficient spectrum can be calculated from Eq. (8), when the drop size distribution and the drop volume fraction are known (forward problem). To calculate the drop size distribution from the measured attenuation coefficients, the reverse problem needs to be solved (Eq. 12.). This is achieved by minimising the difference between measured and calculated attenuation coefficient spectra.

The procedure for obtaining the drop size distribution in a dispersion is summarized as follows: a) measure the attenuation coefficient experimentally in the dispersion for a range of frequencies (Eq. (2)); b) use a mathematical model that can relate the attenuation coefficient, frequency, volume concentration and physical properties with the drop size distribution (Eq. (8)). For this calculation a distribution for the drop sizes (e.g. log-normal) needs to be assumed (for details see Cents et al. (2004); c) minimise the differences between the measured and calculated attenuation coefficients to reduce the error (using Eq.14 below), d) extract the drop size distribution from the measured attenuation coefficient using (Eq. (12)) (Falola et al., 2021).

In this work, the transmitted wave was a pulsed signal with frequencies between 0.5 MHz and 4 MHz. First, the amplitude of the reference signal (A_1) is taken with the vessel filled with the continuous phase (water/glycerol, see Fig.2) at different frequencies, and then the amplitude of the signal transmitted through the dispersion (A_o) is measured. The experimental attenuation coefficients for Cases 1 and 2 are shown in Figs. 3a and b, respectively.

3.2. PLIF

For the PLIF technique a region of interest of approximately 0.6 X D ($1.54 x 103\ mm^2$) was selected in the image, which covers the same area of measurement as that of the ultrasound transducers. The instantaneous images were captured using the full camera resolution and the area of interest was cropped and post-processed with an in-house developed code in MATLAB®. A typical raw image captured by the PLIF technique for Case 1 at 350 rpm is illustrated in Fig.4 (a), with the oil droplets represented by black regions dispersed in the aqueous phase. The technique relies on automatic capturing of the dispersed phase contours in a sequence of images to extract the properties, such as drop size distribution and volume fraction.

Prior to the quantitative measurements, the images were pre-processed based on a background subtraction and a smoothing and equalization procedure using a median intensity filter. This procedure enhances the contrast between the dispersed and continuous phases and eliminates the background noise and static objects from the image. It not only removes any bias that could have been introduced by differences in non-uniform illumination intensity, but also facilitates the determination of a threshold for the binarisation operation, that follows for the identification of drop interface contours. A review of the standard image processing routines is available in (Gonzalez, 2009). The next procedure adopted is the adapt thresh function available in MATLAB® toolbox which chooses the threshold based on the local mean intensity in the neighbourhood of each pixel. This operation automatically detects the edge gradient threshold on drop interfaces and binarises the image. The function *imfindcircles* was applied to recognise drops as circular objects by detecting strong edges in the binarised image. This function detects the drops contour and estimates their centre location and radius considering them as circular objects. As a verification procedure, Fig. 4 (b) illustrates the automatic detection of drops, represented by red circles, overlaid on the original image. As it can be seen, the agreement is excellent. The statistical calculations for drop size distribution and volume fraction were also implemented using routines available in MATLAB®. We assume steady-state concentrations during the data acquisition with an average of number of drops per image varying from 25 to 170, respectively for Case 2 at 350 rpm and Case 1 at 400 rpm. The
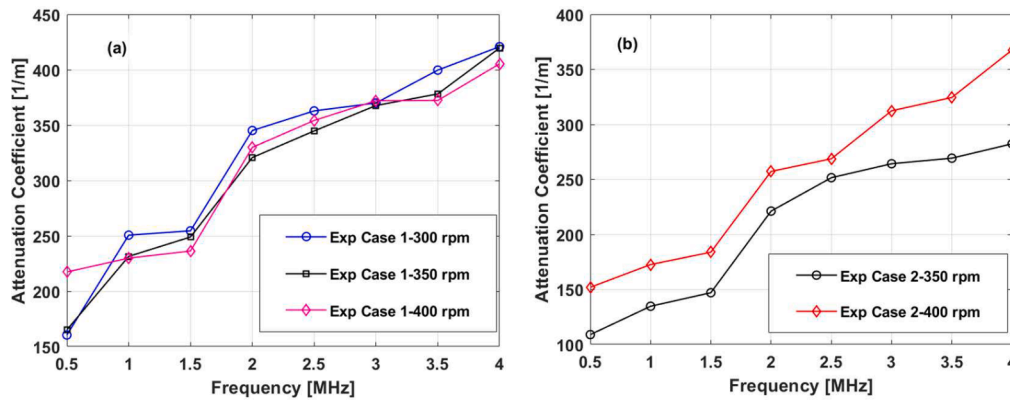
Fig. 3. Ultrasound attenuation coefficient spectra (transmitting signal frequencies x-axis, attenuation coefficient y-axis), a) Case-1 (Impeller positioned at the water/glycerol interface), b) Case-2 (Impeller positioned 25 mm below water/glycerol interface).
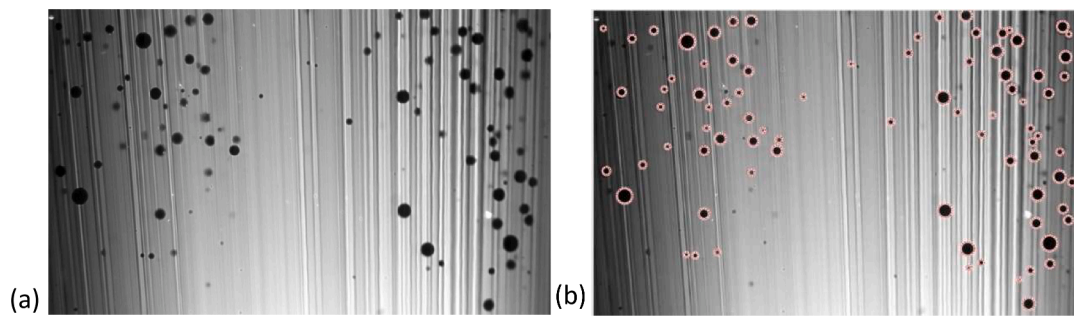

Fig. 4. (a)Typical raw image of Case 1 at 350 rpm capture by PLIF technique. (b)Automated detection of oil droplets (in red) overlapping the original image.

average drop size histogram for each flow condition studied was calculated by an ensemble average of the drop size distribution extracted from all images. The volume fraction, V_f, for each case was determined by the equation below.

$$Vf_{PLIF} = \frac{\sum A_{drop}}{A_{ROI} \cdot N} \quad (13)$$

where, A_{drop} is the measured circular area of each drop calculated by the estimated radius, A_{ROI} is the measuring area of interest, and N is the number of images.

4. Results and discussion

4.1. Droplet volume fraction

To obtain the droplet volume fraction in a dispersion of silicone oil droplets in glycerol/water by ultrasound, three steps were taken: (1) The ultrasound speed was measured with the vessel full with the continuous phase (glycerol/water) only, and it was found equal to $C_{gw} = 1670 m/s$. (2) The sound speed was measured with the vessel filled with the dispersed phase only, and it was found equal to $C_o = 1014 m/s$. (3) The sound speed was measured in the dispersion of silicone oil in glycerol/water for both Case 1 and Case 2 (see Table 2). The droplet volume fractions were calculated from Eq. (3) and the results are shown in Fig. 5 for both cases.

Table 2
Sound speed measured in the dispersion of silicone oil in glycerol/water.

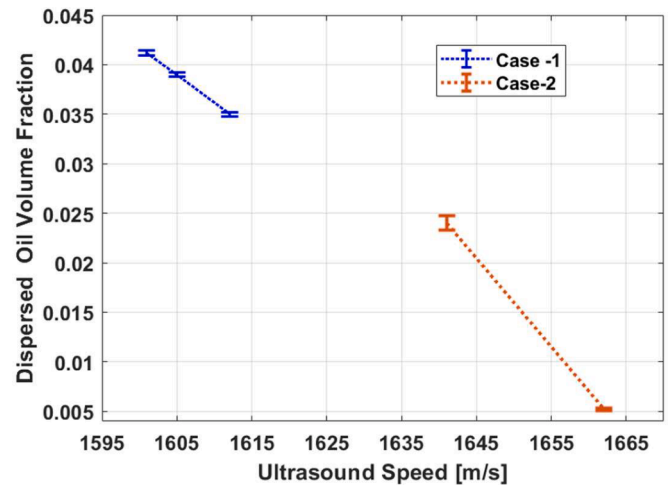| Impeller rotation speed (rpm)	Case 1 (m/s)	Case 2 (m/s)
300	1612	——
350	1605	1662
400	1601	1641

Fig. 5. Silicone oil volume fraction calculated from the measured ultrasound speed in oil in glycerol/water dispersion by using Eq. (3).

In stirred vessel the competition between the drop break up and coalescence determines the drop volume fractions and their size distributions (Liu et al., 2016). The results displayed in Fig. 5 reveal that the sound speed propagation in the mixture is inversely proportional to the oil drop volume fraction, as the ultrasound speed is lower in silicone oil compared to the glycerol/water mixture.

The volume fractions obtained with the ultrasound technique are compared in Fig. 6 with the results from PLIF, obtained at the same time and location. As can be seen, the agreement is excellent between the two techniques even though they are based on different physical phenomena. The results in both Figs. 5 and 6 show that the drop volume
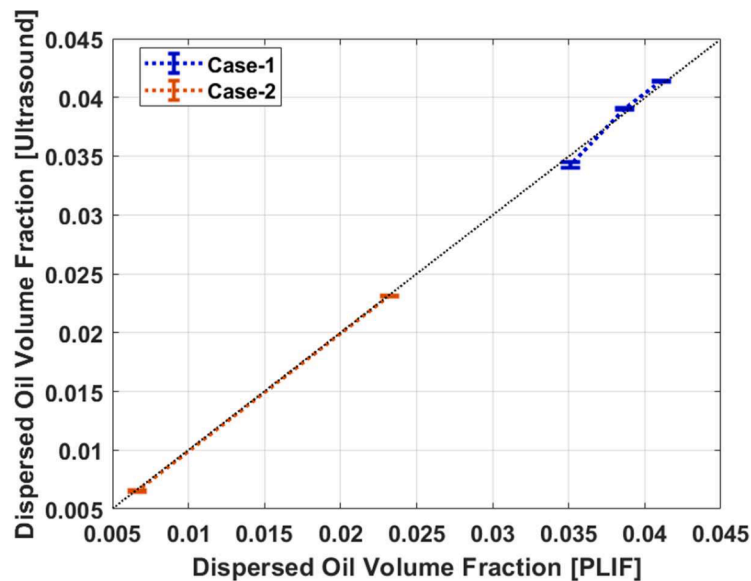
Fig. 6. Silicone oil volume fraction measured by (ultrasound y-axis), and PLIF (x-axis), for the Case 1 (blue diamonds), and for the Case 2 (red circles) plotted with a reference line (dotted) for data comparison.

fractions are larger for Case 1 compared to Case 2. This is because in Case 1 the impeller is located just below the interface, which increases the amount oil that becomes dispersed.

The ultrasound measurements cover the planar area of interest with a depth of approximately equal to the transducer diameter (12.7 mm). As commented previously, PLIF measurements were adjusted with the crop procedure to capture approximately the same planar area, but this technique covers a reduced depth of measurements, that corresponds to the laser plane thickness (1.5 mm). For this reason, laser-based techniques require a large number of images to allow for ensemble average measurements of the dispersed phase properties. In this work, 11,000 images were captured with PLIF for each flow condition. In the same period, eight data sets of ultrasound signals were recorded simultaneously, giving a standard deviation of less than 0.13%.

4.2. Drop size distribution

The flow conditions for the measurement of droplet size distributions with the ultrasound and PLIF techniques are presented in Table 2. The ultrasound attenuation coefficient spectra were measured in the excitation frequency range of 0.5–4 *MHz*, and the inversion method was then used to calculate the droplet size distribution (as described in Section 3.1).

The attenuation coefficients measured for Case 1 and Case 2 were presented in Fig. 3. The experiments were repeated three times, with a standard deviation of 0.24%. The calculation of the drop size distribution is not only related to the frequency and scattering of the ultrasound wave, but also to the choice of the inversion algorithm and the theoretical model. There are few different algorithms available such as the Broyden-Fletcher-Goldfard-Shano (Head and Zerner, 1985), the Levenberg–Marguard (Moré, 1978), and the McClements and Coupland (McClements, 1996). We tested all three models, and the model introduced by McClements and Coupland (1996), which gave the smallest error of 0.7%, was used here; the other two models by Head and Zerner (1985) and Rivard and Bledsoe (1978) gave errors of 3.14% and 5.23% respectively.

As discussed previously, the drop size distribution was calculated from the measured ultrasound attenuation coefficient spectrum using Eq. (12). A log-normal drop size distribution was assumed here for the calculation of the theoretical attenuation coefficient matrix. The final drop size distribution was the one that minimised the error between

measured and calculated attenuation coefficients (Eq. (14)) (Yang et al., 2016):

$$Error = \sqrt{\frac{1}{N}\left(\frac{\alpha_{theoritical} - \alpha_{experimental}}{\alpha_{experimental}}\right)^2} \qquad (14)$$

The drop size distributions obtained for Case 1 for impeller rotational speeds of 300, 350, and 400 rpm and for Case 2 for speeds of 350 and 400 rpm are shown in Fig. 7a and 7b respectively. As it can be seen from Figs. 7a and 7b, in both cases as the impeller speed increases the drop size decreases. In addition, Case 2, with the impeller located further away from the interface, gives smaller drop sizes than Case 1.

The log-normal distribution was assumed in the data post-processing because drop sizes tend to vary over several orders of magnitude. This distribution assumes that most particles are close to the mean, with few particles at large or small sizes, while the logarithmic scale is used to equalise the relative sizes of particles over this large range. It was found that drop sizes larger than 0.2 mm gave the best fit between the measured and the calculated attenuation coefficients. We also tested sizes smaller than 0.2 mm but errors between the measured and calculated attenuation coefficient were found to be larger than 13%.

The amount of scattering (and therefore attenuation) is affected by the drop size r and the wavelength λ of the propagated sound wave. For example when r≫λ (in our case λ was selected in the range of 0.35–3.240 mm) the majority of the wave will be scattered. In the case of r≪λ the scattering of sound is too small to be observed (very low resolution). To obtain, therefore, smaller drop sizes a higher frequency (shorter wavelength) of the propagated sound wave must be used.

Further, the drop size distributions obtained from ultrasound measurements are compared against those obtained from PLIF in Fig. 8 and Fig. 9 for Case 1 and Case 2, respectively. The results are presented in histograms, where the horizontal axis shows the drop size, and the vertical axis is the normalized drop count.

Considering the limitations imposed by their physical mechanisms, each technique can detect a different range for the drop size distribution. As can be seen from Fig. 7, ultrasound was able to capture drops below 0.3 mm, certifying that this technique can interact with small drops and detect them when the sound wavelength is smaller than the drop size. On the other hand, PLIF relies on an image processing tool, *imfindcircles*, available in MATLAB® toolbox with accuracy restricted to detect drops below 10 pixels. For that reason, considering the optical arrangement
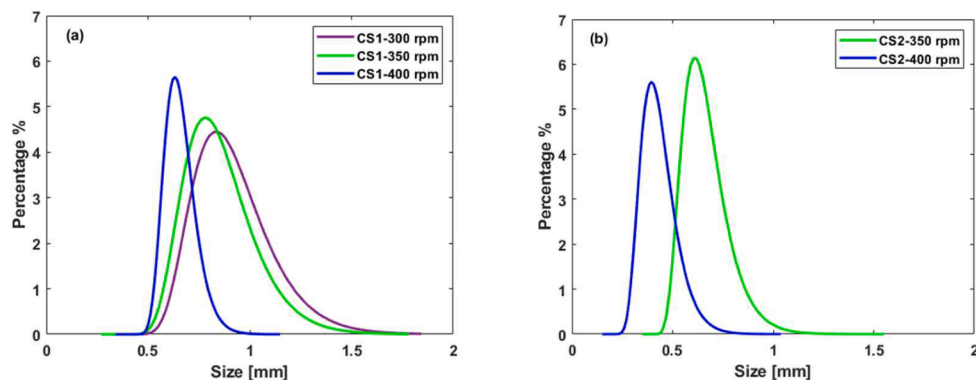
Fig. 7. Inversed drop size distribution from the measured ultrasound attenuation coefficient spectra of silicone oil droplets in water for (a) Case 1 and (b) Case 2.
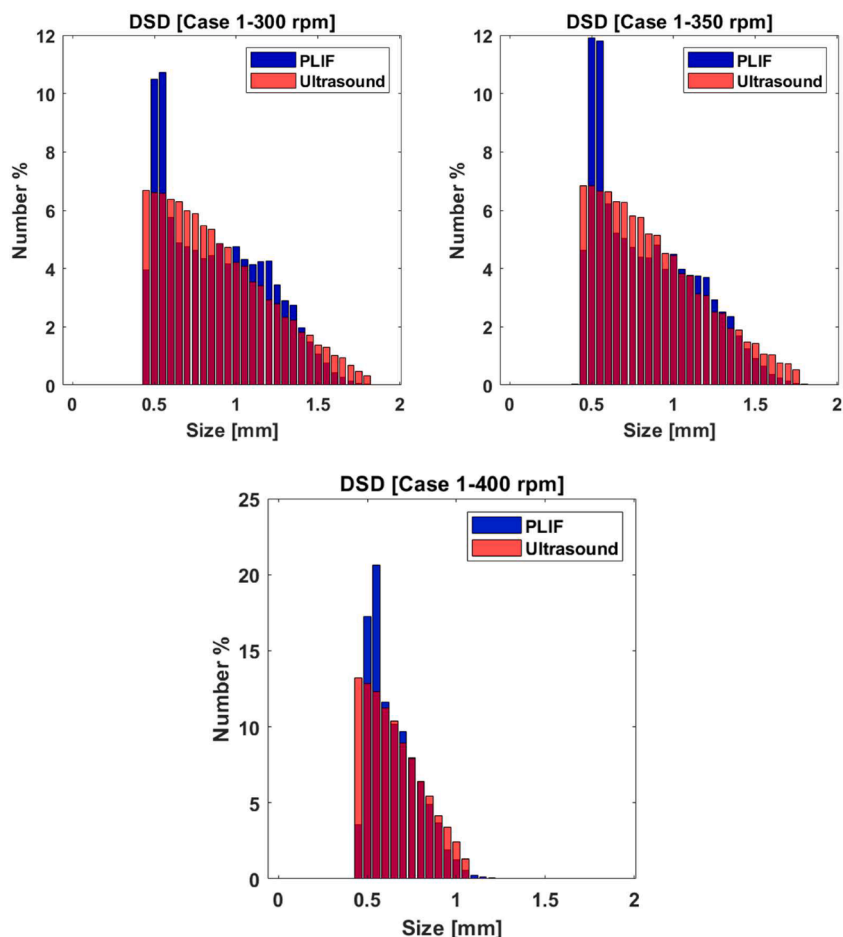

Fig. 8. Inversed drop size distribution from the measured ultrasound attenuation coefficient spectra of silicone oil droplets in water/glycerol with various drop sizes (red bars) and measured drop size distribution (blue bars) by PLIF, for Case 1.

and the image resolution of the present work, PLIF technique is considerably less accurate for detecting drops with diameter smaller than [0.45–0.5] mm. Due to this limitation, very small drops can have their size overestimated or be disregarded by the image post-processing. Small drops are masked as background noise, have less well-defined focus o amount oil that becomes dispersedr brightness contrast, be blurred or hidden behind image refractions and image imperfections. Considering these limitations and to enable comparisons between both techniques, the results shown in Figs. 8 and 9 are normalized histograms with the same drop size range, starting from 0.45 mm of diameter. It is important to note that Fig. 8 is not directly produced from Fig. 7. This is

because the PLIF analysis revealed a half log-normal distribution of the drop sizes, not a full log-normal distribution as depicted in Fig. 8. Therefore, when comparing the drop sizes measured by ultrasound (US) with those measured by PLIF, we processed the US data using a half log-normal function available in MATLAB, discretized the data, and then compared the drop sizes measured by both techniques.

The results reported by both techniques show that drop size distributions shift to smaller values as the impeller speed increases for both Cases 1 and Case 2. In addition, larger drops are observed for Case 1, where the impeller is located just below the interface. The results are in accordance with literature findings on dispersions formed in stirred
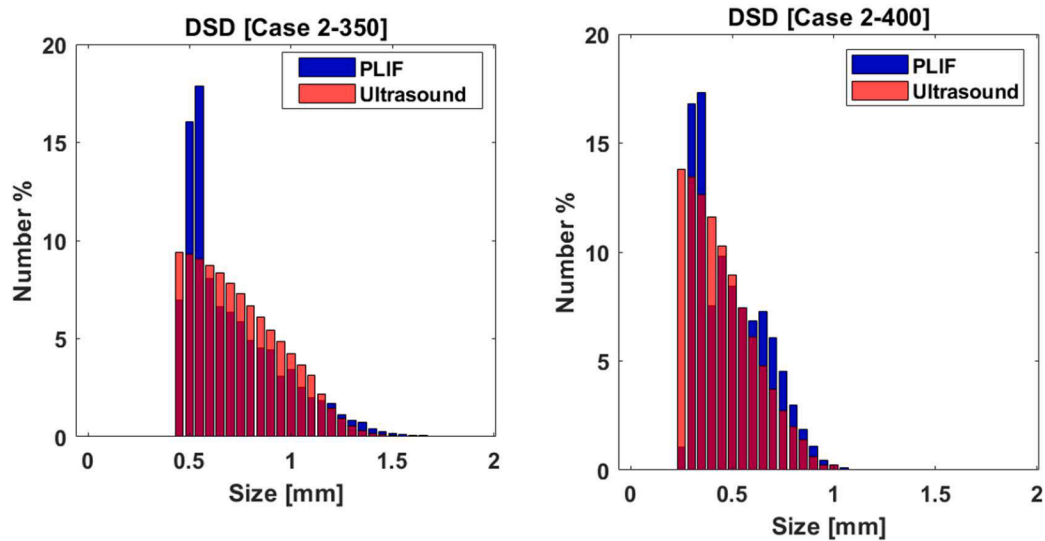
Fig. 9. Inversed droplet size distribution from the measured attenuation coefficient of silicone oil droplets in water/glycerol with various drop sizes [red bars] and measured drop size distribution [blue bars] by PLIF, for Case 2.

vessels (Liu et al., 2016), which indicate that increasing impeller rotational speed is leading to increased drop break up and decreased drop size.

The results from the PLIF technique show for all cases a higher concentration of drops at smaller sizes; in particular PLIF gives a peak at the second and third drop size bins. Considering that this same tendency is observed for all five cases, the difference between both techniques indicates that the image processing applied for the PLIF technique overestimated the sizes of the small drops. These drops have diameter smaller than the size limitation imposed by the image processing tool for an accurate detection.

The difference on drop size distribution reported between PLIF and ultrasound techniques at larger drop sizes for Case 1 at 300 and 350 rpm and Case 2 for 400, is attributed to the differences between drop size calculation mechanisms. The drop sizes measured with PLIF are in fact chord lengths, depending on the part of the drop that is cut by the laser plane. It has been shown that for spherical drops, the measured chord length distributions are biased to larger sizes compared to the equivalent drop diameter distribution (Hu et al., 2006). In the present work it was observed that the PLIF technique can, therefore, overestimate the drop diameter towards larger sizes than ultrasound.

5. Conclusions

Ultrasound techniques are a category of acoustic methods and can be used for the characterisation of dispersed systems when the continuous phase is a liquid. In this work, the ultrasound techniques were developed to measure volume fraction and drop size distribution in dispersed liquid-liquid flows. The volume fraction was obtained from the speed of sound through the dispersion. The drop size distribution was calculated from measurements of the sound wave attenuation as it travels through the dispersed medium and the application of an inversion algorithm. It was found that the ultrasound speed is inversely proportional to the silicone oil volume fraction. For the validation of the ultrasound results,

a Planar Laser Induced Fluorescence (PLIF) technique was used to capture time resolved images of the dispersion at the same time and location as that of the ultrasound transducers.

For the experiments, silicon oil and a glycerol/water mixture were used as test fluids. The experimental set up consisted of a cylindrical stirred vessel with the impeller located either just below the interface or at 25 mm below it, in the glycerol/water solution. The volume fractions of the dispersed oil phase were in excellent agreement between the ultrasound and the PLIF techniques. There was a good agreement also on the drop size distributions between the two techniques. The differences were explained in terms of limitations of the optical technique.

The above results indicate that ultrasound techniques are a powerful tool for the characterisation of dispersed liquid-liquid flows. They provide fast results, which will be valuable for online measurements. In addition, ultrasound techniques are feasible for optically non-transparent test sections.

Declaration of Competing Interest

The authors declare that they have no known competing financial interests or personal relationships that could have appeared to influence the work reported in this paper.

Data availability

Data will be made available on request.

Appendix I

The volume fraction of oil in the dispersion of oil V_o, and glycerol/water V_{gw} can be given by:

$$\varphi = \left(\frac{V_o}{V_o + V_{gw}} \right) \tag{A1}$$

From the mass conversation of dispersed and continuous phase we can get:

$$\rho\left(V_o + V_{gw}\right) = \rho_o V_o + \rho_{gw} V_{gw} \tag{A2}$$

$$\rho = \frac{\left(\rho_o V_o + \rho_{gw} V_{gw}\right)}{\left(V_o + V_{gw}\right)} = \rho_o \varphi + \rho_{gw}(1 - \varphi) \tag{A3}$$

If both sides of Eq.3 divided by ρ_{gw} we get:

$$\frac{\rho}{\rho_{gw}} = \frac{\rho_o \varphi}{\rho_{gw}} + (1 - \varphi) = (1 - \varphi)(1 - r) \tag{A4}$$

Were, $r = \frac{\rho_o}{\rho_{gw}}$,

$$C_o = \frac{1}{\sqrt{k_o \rho_o}}, \ C_{gw} = \frac{1}{\sqrt{k_{gw} \rho_{gw}}}, \ C = \frac{1}{\sqrt{k\rho}} \tag{A5}$$

$$\frac{k_o}{k_{gw}} = \frac{k_o}{k_{gw}} \frac{\rho_o}{\rho_{gw}} \frac{\rho_{gw}}{\rho_o} = \frac{C_{gw}^2}{rC_o^2} = \frac{C_1}{rC_2}$$

Here, $C_1 = \frac{C^2}{C_o^2}$, and $C_2 = \frac{C^2}{C_{gw}^2}$

$$k = \varphi k_o + (1 - \varphi)k_{gw} \tag{A6}$$

$$\frac{k}{k_{gw}} = \frac{\varphi k_o}{k_{gw}} + (1 - \varphi) = 1 - \varphi\left(1 - \frac{C_1}{rC_2}\right) \tag{A7}$$

The following Eq.8 was found from Eq.7, Eq6, and eq.4:

$$\varphi = \frac{-B \pm \sqrt{B^2 - 4AD}}{2A} \tag{A8}$$

$$A = \left(\left(\frac{C^2}{C_g^2}\right) - \frac{\rho_o}{\rho_{gw}}\left(\frac{C^2}{C_{gw}^2}\right)\right)\left(1 - \frac{\rho_o}{\rho_{gw}}\right)$$

$$B = 2\frac{\rho_o}{\rho_{gw}}\left(\frac{C^2}{C_{gw}^2}\right) - \left(\frac{C^2}{C_o^2}\right) + \left(\frac{\rho_o}{\rho_{gw}}\right)^2\left(\frac{C^2}{C_{gw}^2}\right) + 2\frac{\rho_o}{\rho_{gw}}\left(1 - \left(\frac{C^2}{C_o^2}\right) - \frac{\rho_o}{\rho_{gw}}\right)$$

$$D = \frac{\rho_o}{\rho_{gw}}\left(1 + 2\frac{\rho_o}{\rho_{gw}}\right)\left(1 - \left(\frac{C^2}{C_{gw}^2}\right)\right)$$

Appendix II

In the dispersion system, scattering of ultrasound wave is the paramount interactions between the droplet and the ultrasonic wave. A simplified scattering coefficient expressed by (McClements, 1996), and is given by:

$$A_n = \frac{\rho_1 a j_n'(a)j_n'(a) - \rho_2 a j_n'(a)j_n'(a)}{\rho_2 a j_n'(a)j_n(a) - \rho_1 a j_n'(a)h_n(a)} \tag{B1}$$

Where $a = k.r$, and j_n is spherical Bessel function, and h_n is spherical Hankel function, and the subscribes are referring to the first derivatives of the associated parameters.

References

Angeli, P., Tsaoulidis, D., Weheliye, W.H., 2019. Studies on mass transfer of europium (III) in micro-channels using a micro laser induced fluorescence technique. Chem. Eng. J. 372, 1154–1163.

Atkinson, P., Wells, P.N., 1977. Pulse-Doppler ultrasound and its clinical application. Yale J. Biol. Med. 50, 367.

Ayala, J.S., De Moura, H.L., Amaral, R.D.L., Oliveira Jr., F.D.A., Nunhez, J.R., De Castilho, G.J., 2022. Two-dimensional shear rate field and flow structures of a pseudoplastic fluid in a stirred tank using particle image velocimetry. Chem. Eng. Sci. 248, 117198.

Bieberle, A., Härting, H.U., Rabha, S., Schubert, M., Hampel, U, 2013. Gamma-ray computed tomography for imaging of multiphase flows. Chem. Ing. Tech. 85, 1002–1011.

Bouillard, J., Alban, B., Jacques, P., Xuereb, C., 2001. Liquid flow velocity measurements in stirred tanks by ultra-sound doppler velocimetry. Chem. Eng. Sci. 56, 747–754.

Bowler, A.L., Bakalis, S., Watson, N.J., 2020. A review of in-line and on-line measurement techniques to monitor industrial mixing processes. Chem. Eng. Res. Des. 153, 463–495.

CHAROGIANNIS, A. & MARKIDES, C.N. 2014. Experimental study of falling films by simultaneous laser-induced fluorescence, particle image velocimetry and particle tracking velocimetry.

Castellano, S., Carrillo, L., Sheibat-othman, N., Marchisio, D., Buffo, A., Charton, S., 2019. Using the full turbulence spectrum for describing droplet coalescence and breakage in industrial liquid-liquid systems: experiments and modeling. Chem. Eng. J. 374, 1420–1432.

Cents, A., Brilman, D.W.F., Versteeg, G., Wijnstra, P., Regtien, P.P., 2004. Measuring bubble, drop and particle sizes in multiphase systems with ultrasound. AlChE J. 50, 2750–2762.

Charogiannis, A., Sik An, J., Voulgaropoulos, V., Markides, C.N., 2019. Structured planar laser-induced fluorescence (S-PLIF) for the accurate identification of interfaces in multiphase flows. Int. J. Multiphase Flow 118, 193–204.

Dong, X., Tan, C., Yuan, Y., Dong, F., 2015. Oil–water two-phase flow velocity measurement with continuous wave ultrasound Doppler. Chem. Eng. Sci. 135, 155–165.

Falola, A.A., Huang, M.X., Zou, X.W., Wang, X.Z., 2021. Characterization of particle size distribution in slurries using ultrasonic attenuation spectroscopy: addressing challenges of unknown physical properties. Powder Technol. 392, 394–401. D.

Farias, P.S.C., Martins, F.J.W.A., Sampaio, L.E.B., Serfaty, R., Azevedo, L.F.A., 2012. Liquid film characterization in horizontal, annular, two-phase, gas–liquid flow using time-resolved laser-induced fluorescence. Exp. Fluids 52, 633–645.

Gonzalez, R.C., 2009. Digital Image Processing. Pearson education, India.

Head, J.D., Zerner, M.C., 1985. A Broyden—Fletcher—Goldfarb—Shanno optimization procedure for molecular geometries. Chem. Phys. Lett. 122, 264–270.

Hossein, F., Wang, M., 2020. Modelling and measurement of ultrasound vibration potential distribution in an agar phantom. Chem. Phys. 534, 110757.

Hossein, F., Materazzi, M., Lettieri, P., Angeli, P., 2021. Application of acoustic techniques to fluid-particle systems–A review. Chem. Eng. Res. Des. 176, 180–193.

Hossein, F., Materazzi, M., Errigo, M., Angeli, P., Lettieri, P., 2022. Application of ultrasound techniques in solid-liquid fluidized bed. Measurement, 111017.

Hossein, F., 2019. Colloid Vibration Potential For Imaging in Engineering and Medicine. University of Leeds.

Hu, B., Angeli, P., Matar, O.K., Lawrence, C.J., Hewitt, G.F., 2006. Evaluation of drop size distribution from chord length measurements. AIChE J. 52, 931–939.

Iannello, S., Morrin, S., Materazzi, M., 2020. Fluidised bed reactors for the thermochemical conversion of biomass and waste. Kona 37, 114–131.

Jia, N., Su, M.-X., Cai, X.-S., 2019. Particle size distribution measurement based on ultrasonic attenuation spectra using burst superposed wave. Results in Phys. 13, 102273.

Kikuchi, Y., Kanagawa, T., Ayukai, T., 2022. Physico-mathematical model for multiple ultrasound-contrast-agent microbubbles encapsulated by a visco-elastic shell: effect of shell compressibility on ultrasound attenuation. Chem. Eng. Sci., 117541

Liu, N., Wang, W., Han, J., Zhang, M., Angeli, P., Wu, C., Gong, J., 2016. A PIV investigation of the effect of disperse phase fraction on the turbulence characteristics of liquid–liquid mixing in a stirred tank. Chem. Eng. Sci. 152, 528–546.

Martínez, A.N.M., Assirelli, M., Van Der Schaaf, J., 2021. Droplet size and liquid-liquid mass transfer with reaction in a rotor-stator spinning disk reactor. Chem. Eng. Sci. 242, 116706.

Mcclements, D.J., 1996. Principles of ultrasonic droplet size determination in emulsions. Langmuir 12, 3454–3461.

Moré, J.J, 1978. The Levenberg-Marquardt algorithm: implementation and theory. Numerical Analysis. Springer.

Murakawa, H., Ichimura, S., Sugimoto, K., Asano, H., Umezawa, S., Sugita, K., 2020. Evaluation method of transit time difference for clamp-on ultrasonic flowmeters in two-phase flows. Exp. Therm Fluid Sci. 112, 109957.

Povey, M.J.W., 2013. Ultrasound particle sizing: a review. Particuology 11, 135–147.

Prakash, B., Parmar, H., Shah, M.T., Pareek, V.K., Anthony, L., Utikar, R.P., 2019. Simultaneous measurements of two phases using an optical probe. Exp. Comput. Multiph. Flow 1, 233–241.

Rave, K., Hermes, M., Wirz, D., Hundshagen, M., Friebel, A., Von, Harbou, Bart, H.-J., Skoda, R., 2022. Experiments and fully transient coupled CFD-PBM 3D flow simulations of disperse liquid-liquid flow in a baffled stirred tank. Chem. Eng. Sci. 253, 117518.

Riebel, U., LÖffler, F, 1989. The fundamentals of particle size analysis by means of ultrasonic spectrometry. Particle Particle Sys. Character. 6, 135–143.

Rivard, D., Bledsoe, L., 1978. Production model under nonequilibriumconditions. Fish. bull. 76, 523.

Rodriguez, O.M.H., Rodriguez, I.H., Ansoni, J.L., 2019. An experimental and numerical study on the wall lubrication force in dispersed liquid-liquid flow. Int. J. Multiphase Flow 120, 103094.

Rodríguez, D.J., Shedd, T.A., 2004. Entrainment of gas in the liquid film of horizontal, annular, two-phase flow. Int. J. Multiphase Flow 30, 565–583.

Russell, A.W., Kahouadji, L., Mirpuri, K., Quarmby, A., Piccione, P.M., Matar, O.K., Luckham, P.F., Markides, C.N., 2019. Mixing viscoplastic fluids in stirred vessels over multiple scales: a combined experimental and CFD approach. Chem. Eng. Sci. 208, 115129.

Simmons, M.J.H., Hanratty, T.J., 2001. Droplet size measurements in horizontal annular gas–liquid flow. Int. J. Multiphase Flow 27, 861–883.

Su, M., Xue, M., Cai, X., Shang, Z., Xu, F., 2008. Particle size characterization by ultrasonic attenuation spectra. Particuology 6, 276–281.

Tas-Koehler, S., Neumann-Kipping, M., Liao, Y., Bieberle, A., Hampel, U., 2022. Experimental investigations and numerical assessment of liquid velocity profiles and turbulence for single- and two-phase flow in a constricted vertical pipe. Int. J. Multiphase Flow 157, 104224.

Urick, R., 1947. A sound velocity method for determining the compressibility of finely divided substances. J. Appl. Phys. 18, 983–987.

Vauhkonen, M., Hänninen, A., Jauhiainen, J., Lehtikangas, O, 2019. Multimodal imaging of multiphase flows with electromagnetic flow tomography and electrical tomography. Meas. Sci. Technol. 30, 094001.

Wallace, L., Lucieer, A., Watson, C., Turner, D., 2012. Development of a UAV-LiDAR system with application to forest inventory. Remote. Sens. 4, 1519–1543.

Wang, W., Gong, J., Angeli, P., 2011. Investigation on heavy crude-water two phase flow and related flow characteristics. Int. J. Multiphase Flow 37, 1156–1164.

Waterman, P.C., Truell, R., 1961. Multiple scattering of waves. J. Math. Phys. 2, 512–537.

Wu, H., BUSCHLE, B., Yang, Y., Tan, C., Dong, F., Jia, J., Lucquiaud, M., 2018. Liquid distribution and hold-up measurement in counter current flow packed column by electrical capacitance tomography. Chem. Eng. J. 353, 519–532.

Yang, H., Su, M., Wang, X., Gu, J., Cai, X., 2016. Particle sizing with improved genetic algorithm by ultrasound attenuation spectroscopy. Powder Technol. 304, 20–26.

Yelpale, M., Shrivastava, R., Nandan, G., 2021. Heat Transfer Enhancement and Pressure Drop in Two-Phase Flow Boiling Using Coiled Wire as Turbulent promoters: A review. American Institute of Physics, Melville.